Dislocation pinning by glissile interstitial loops in a nickel crystal: A molecular-dynamics study

D. Rodney and G. Martin
Section de Recherches de Métallurgie Physique, CEA/Saclay, 91191 Gif-sur-Yvette, France
(Received 20 September 1999)

Molecular-dynamics simulations show that, in an embedded-atom method nickel crystal, interstitial loops made of $\langle 110 \rangle$ dumbbells may be absorbed by an edge dislocation in two different ways, either being attached to one of the Shockley partials by means of a dislocation junction or being transformed into a double superjog on the dislocation. In both cases, the absorption is assisted by a flip of the loop Burgers vector. The simulations also show that double superjogs lock the dislocation but are only weak obstacles. In all cases, the loops may be dragged by the dislocation and induce on the latter an additional friction which is evaluated from the simulations.

I. INTRODUCTION

Irradiation induced hardening of metals and alloys is known experimentally since the 1950s (Refs. 1 and 2) and is characterized by an increase of the yield stress of irradiated materials with increasing irradiation dose and decreasing irradiation temperature.

The increase in yield stress is due to the interactions of the dislocations responsible for the plastic deformation with the irradiation defects, and among them, mainly with the interstitial loops.[3]

Long-range interactions between a dislocation and an interstitial loop have been studied in the 1960s by means of the elastic theory of dislocations.[4–6] Short-range reactions have been observed in transmission electron microscopy (TEM) (for a review, see Ref. 7) and classified, depending on the geometry of the interstitial loop and of the dislocation.[8,7] A particularity of these processes is that the Burgers vector of the loop may change during the interaction, leading, for example, to the unfaulting of Frank loops,[9] or to the absorption of the loops as *helicoidal turns* on screw dislocations.[10,7]

Less is known about the pinning effect of the irradiation defects. For this reason, the hardening mechanisms are still open to discussion. Two main mechanisms have been proposed. The first one is the *dispersed barrier hardening*,[11] where irradiation defects act individually as barriers to the motion of the dislocations. In the second mechanism, called *source hardening*,[2] irradiation defects are not barriers by themselves. They lock the dislocations present in the crystal during the irradiation by gathering around them and forming *defect clouds*. Since these dislocations are the Frank Read sources for the dislocations necessary to the plastic deformation, the latter cannot be initiated until a stress sufficient to free the sources is applied, leading to an increase in the yield stress of the material. Experimental observations support both mechanisms. On the one hand, traction tests show that the yield stress increases as the square root of the defect density,[3] which is expected with the dispersed barrier mechanism. On the other hand, dislocations decorated by defect clouds have been observed in TEM,[12] and the mechanical instability, which occurs just after initiation of the plastic deformation in irradiated materials (and corresponds to the formation and propagation of shear bands) is a direct consequence of source hardening.[13]

In the last decade, molecular-dynamics (MD) simulations of displacement cascades gave new insights with respect to defect clustering under irradiation. The simulations showed that in fcc metals, a significant fraction of the interstitials is produced as small clusters, made of less than a few tens of $\langle 110 \rangle$ dumbbell interstitials.[14,15] In terms of dislocations, these clusters are small perfect interstitial loops with $a/2\langle 110 \rangle$ Burgers vectors. Similar loops also form in simulations of, for example, hcp α-zirconium, bcc α-iron, and of $L1_2$ Ni_3Al alloys.[16,17] The reason for the clustering is still unclear. Clusters may form by coalescence of isolated interstitials, produced in localized regions at the periphery of displacement cascades.[15] But large interstitial clusters may also form spontaneously, as a result of collective events, possibly induced by the high shear stresses which develop during the cascades.[18] Interstitial clusters have been studied at the atomic scale in various fcc metals using different interatomic potentials.[19,20] Their main characteristic is to be highly mobile along their glide cylinder in the direction of their Burgers vector. Their direct observation in TEM has only been possible for loops of radius greater than 1 nm,[21] where their one-dimensional glide has been confirmed.

Recently, Trinkaus, Singh, and Foreman[12,22] proposed that such interstitial clusters could play a major role in source hardening, since they can glide over large distances and be trapped in the strain field of dislocations, resulting in the formation of defect clouds. The above analysis was, however, based on elasticity theory.

In order to better understand the role of these small glissile interstitial loops in irradiation hardening, we have undertaken an atomistic study of their pinning effect on a perfect edge dislocation, in an embedded-atom method (EAM) fcc nickel crystal. Preliminary results were presented elsewhere.[23] In the present paper, we consider clusters of different sizes, initially placed either below or ahead of the dislocation. Our aim is twofold. First, we characterize, at the atomic level, the short-range processes that occur when a glissile loop comes into contact with the edge dislocation. Second, we examine the resistance offered by the loops to the glide of the dislocation. In particular, we evaluate from the simulations, both the critical stress to unpin the dislocation and the increase in viscous friction caused by absorbed loops on the gliding dislocation.

The paper is organized as follows. In Sec. II, we present the atomic-level methods employed in this work. The statics and dynamics of the edge dislocation and of the interstitial

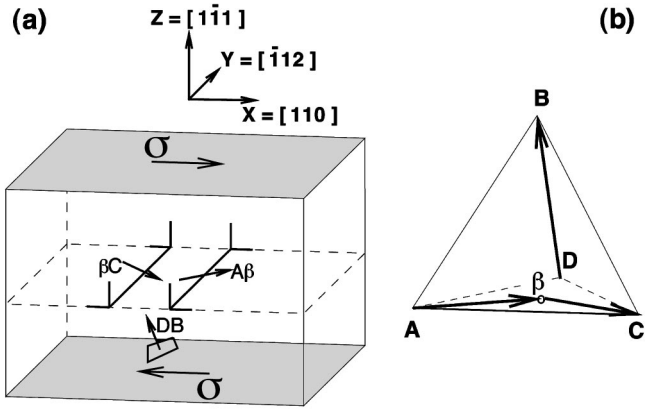

FIG. 1. Schematic view of the simulation cell (a) and corresponding Thompson tetrahedron (b). The origin of the coordinate system is taken at the center of the cell.

clusters, considered separately, are discussed in Sec. III. The results of the simulations on the behavior of the clusters in presence of the dislocation, are presented in Secs. IV and V. Finally, we discuss the implications of simulations with respect to irradiation hardening in Sec. VI and conclude in Sec. VII.

II. METHODOLOGY

A. Simulation methods and interatomic potentials

The simulations performed here are either MD simulations at finite temperature or static zero-temperature energy minimizations. Time is integrated, in the MD simulations, using Verlet algorithm with a time step between 0.5 and 2×10^{-15} s, depending on the temperature. The simulations are performed at constant temperature and applied stress, in a way described in the next section. When static equilibrium configurations are of interest, the potential energy stored in the simulation cell is minimized using a conjugate gradient (CG) routine.

Two embedded-atom method (EAM) potentials, developed to simulate nickel crystals, are used. If not explicitly specified, the simulations described here are performed using the potential developed by Angelo, Moody, and Baskes to simulate dislocations[24] and dislocation junctions in two dimensions.[25] A second potential, developed recently by Mishin *et al.*[26] was also employed, in order to check the sensitivity of the simulations on the interatomic potential.

B. Simulation cell and boundary conditions

The cell used for all simulations is sketched in Fig. 1, along with a Thompson tetrahedron showing its crystallographic orientation. Throughout this paper, the notations used for the dislocation Burgers vectors are taken according to this tetrahedron.

The crystallographic orientation was chosen such that a perfect edge $a/2[110](1\bar{1}1)$ dislocation may initially be introduced between the two central $(1\bar{1}1)$ planes of the cell, with a line along the central $Y=[\bar{1}12]$ axis, and an **AC** Burgers vector along the $X=[110]$ axis.

Two cells have mainly been used: a small one, of dimensions $10\times8.5\times6$ nm and a large one, of dimensions $20\times17\times6$ nm. They contain, respectively, 5×10^4 and 2×10^5 atoms.

The boundary conditions used in the present work are adapted from those employed by Daw and co-workers[27,28] to study dislocation dynamics. Periodic boundary conditions are applied in the X and Y directions such that an array of infinite parallel dislocations is simulated. We apply, in the Z direction, modified free boundary conditions: the atoms lying in the upper and lower (111) surfaces are constrained to two-dimensional dynamics and are fixed in the Z direction. Similar conditions have been used in static simulations[29] and allow for atomic relaxations inside the surfaces both when the dislocation is at rest and when it moves in its glide plane.

The MD simulations are performed at constant temperature and constant applied stress. An initial temperature is applied to a static equilibrium configuration by setting the initial atomic velocities according to a Maxwellian distribution. The temperature is then maintained fixed by periodically rescaling the velocities every 100 time steps.[30] By using different initial distributions of atomic velocities, different dynamical trajectories corresponding to a given temperature may be investigated.

A constant shear stress σ_{xz} may be applied to the simulation cell by superimposing constant forces in the $[110]$ direction to the forces felt by the atoms in the outer $(1\bar{1}1)$ surfaces, as shown in Fig. 1(a). The forces in the upper and lower surfaces have opposite directions and the upper force is scaled to account for the presence of the two extra (110) half planes introduced by the edge dislocation. The stress σ_{xz} ranges from 7.5 to 300 Mpa, which corresponds to stresses from 0.006 to 0.24% of C_{44}, the shear modulus.

C. Visualization methods

Simulation results are visualized using two methods. Static equilibrium configurations, obtained after energy minimization, are shown by plotting only those atoms which energy is at least 0.07 eV above the atomic cohesive energy. This threshold energy allows to extract only the atoms lying in the core of the partial dislocations and of the interstitial loops.

This method leads to noisy results when applied to dynamical configurations. In this case, we take advantage of the fact that the dislocation glide plane is known. The atomic environment of the atoms lying in this plane is compared to fcc and hcp perfect environments. It is known that away from the dislocation extended core, the stacking is fcc and inside the stacking fault ribbon, it is hcp. Therefore if the local environment of an atom is neither close to fcc nor to hcp, the latter is visualized, as being part of a *disturbed* region. This method proved to be very efficient, since it allows to extract the atoms in the cores of the partials and of the loops, both in static and in dynamic configurations.

III. DISLOCATION AND INTERSTITIAL CLUSTERS ALONE

We consider first the dislocation and the interstitial clusters separately and examine successively their static equilibrium configuration and their dynamics.

A. Edge dislocation

1. Static equilibrium configuration

The edge $a/2[110](1\bar{1}1)$ dislocation is introduced by displacing all atoms in the simulation cell, according to the elastic displacement field of the corresponding undissociated dislocation. Its two extra (110) half planes are initially placed on the left-hand (110) face of the cell. They extend from the top $(1\bar{1}1)$ surface down to the plane $z=+a/2\sqrt{3}$. The $(1\bar{1}1)$ plane just below, at $z=-a/2\sqrt{3}$, is referred to, in the present article, as the *dislocation glide plane*.

Atoms lying in the $(1\bar{1}1)$ surfaces are not displaced in the Z direction, so that these surfaces remain flat initially and also throughout the simulations, because of the two-dimensional (2D) boundary conditions chosen for the present study.

After application of the elastic displacements, the X dimension of the cell is close to $L_x+b/2$, where L_x was its initial dimension. In order to account for this expansion, necessary to the elastic equilibrium of the initial dislocation, the periodic length in the X direction is set to $L_x+b/2$. We also note that application of periodic boundary conditions in the X direction cancels the lattice rotation normally associated with an edge dislocation. These boundary conditions are equivalent to equal and opposite couples applied on the (110) surfaces, that balance the lattice rotation. These couples, as well as the forces equivalent to the 2D boundary conditions, influence the dislocation and the interstitial clusters. However, it has been shown by using cells of different sizes that the atomic-level processes occurring during the simulations, which are the main subject of the present article, are unaffected by these boundary conditions.

An initial CG energy minimization allows the dislocation to dissociate in its glide plane into two Shockley partials with Burgers vectors $\mathbf{A}\beta$ and $\beta\mathbf{C}$ [according to Fig. 1(b)]. The dissociation distance depends on the potential used: in the large simulation cell, it is equal to 3.4 nm with Angelo's potential, and 2.4 nm with Mishin's. The dissociation is independent of the cell dimensions in the Y and Z directions but depends on the dimension in the X direction: in the small cell, it is equal to 2.7 and 2.2 nm with Angelo's and Mishin's potentials, respectively. This dependence, which remains small, is a first manifestation of the influence of the periodic boundary conditions applied in the X direction.

The larger dissociation distance obtained with Angelo's potential is due to the smaller stacking fault energy predicted by this potential (89 $\mathrm{mJ\,m^{-2}}$ instead of 125 $\mathrm{mJ\,m^{-2}}$ with the other potential). It remains, however, within the range of dissociation distances observed experimentally in TEM, since Carter and Homes,[31] whose observations were used to evaluate the stacking fault energy in nickel crystals, report dissociation distances of edge dislocations in such crystals between 1.8 and 3.6 nm.

Dislocations in real specimens contain jogs, which are known to absorb interstitials, leading to dislocation climb. In order to study the dynamics of such absorptions, a dislocation with a double jog was considered. The height of the jogs is equal to one interplanar spacing, i.e., they are unit jogs. A pair of jogs of opposite signs was required by the periodic boundary conditions applied along the dislocation line. The dislocation is introduced in the large cell by breaking its initial line into two parts: a first part, which corresponds to $|y|>L_y/4$, runs as before between the two central $(1\bar{1}1)$ planes of the cell. The second part, corresponding to $|y|<L_y/4$, runs between the two planes just above, i.e., between $z=a/2\sqrt{3}$ and $z=a/2\sqrt{3}+a/\sqrt{3}$. The two glide planes are called, respectively, the lower and the upper glide planes. The relaxed configuration is presented in Fig. 2, where only energetic atoms are shown. Atoms which belong to the partials in the lower and the upper glide plane appear in white and gray, respectively.

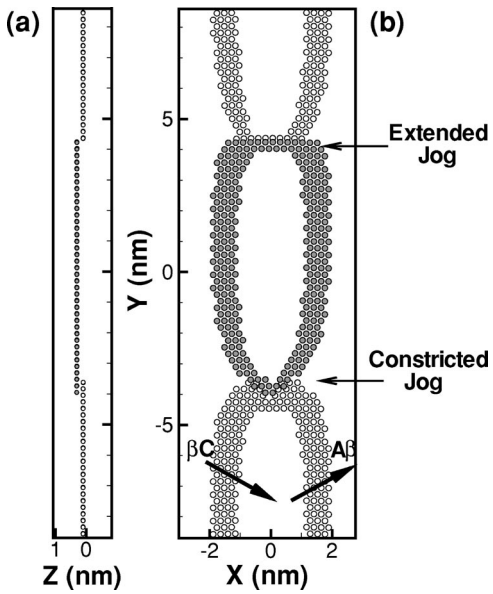

FIG. 2. Relaxed structure of the jogged dislocation seen in the X direction (a) and Z direction (b). Atoms in the lower and upper glide planes appear, respectively, in white and gray.

The two jogs are not identical, one being extended, and the other constricted, as noted in Fig. 2(b). Similar structures have been observed with TEM in copper-aluminum alloys.[32] It may be explained by the different nature, and therefore different line tensions, of the stair-rod dislocations that form along the jogs.

The structure of a jogged dislocation is discussed in Ref. 33 in the case of *superjogs*, i.e., jogs with a height greater than the interplanar spacing. Jogs on edge dislocations are small glissile dislocation segments which can dissociate in their {111} glide plane [the ABC plane in the present case, according to the notations of Fig. 1(b)]. Dissociation leads to the formation of a dipole of stair-rod dislocations along the two **AC** [110] lines of intersection between the main glide plane and the glide plane of the jogs. The nature of the stair rods depends on the jogs: $\delta\beta$ Lomer-Cottrell segments are created along the extended jog while $\delta\beta/\mathbf{AC}$ stair rods form along the other jog (according to the notations used in Ref. 33). The former segments, having a short Burgers vector (of norm $a/3\sqrt{2}$), have a low line tension (proportional to the Burgers vector squared) and are energetically favorable and lead to the extension of the jog. The latter segments have a longer Burgers vector (of norm $a/3$), which forces the jog to remain constricted. Since the jogs in the present case have a height equal only to one interplanar spacing, application of such elastic arguments may be questionable. However, Fig. 2

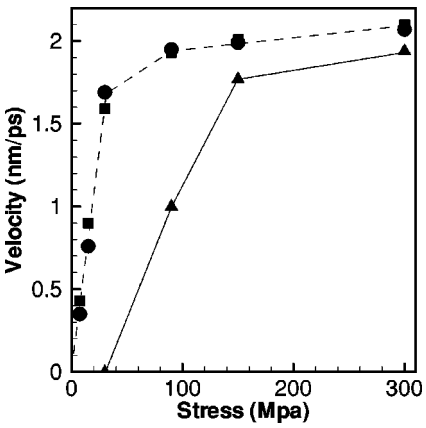

FIG. 3. Dislocation velocity as a function of applied stress at 100 K. The dashed and solid curves correspond, respectively, to the free and the jogged dislocations. Circles and triangles were obtained in the large cell, squares in the small cell.

shows that they explain the general structure of the jogged dislocation. A similar structure will be examined in a later section, where it is shown that an interstitial loop may be absorbed by the dislocation in the form of a pair of superjogs.

An effect of the anisotropy of the line tension of the partial dislocations is also visible in Fig. 2. Similar effects have been observed on extended dislocations intersecting a free surface both in TEM (Ref. 32) and MD simulations.[34] They lead in the present case to a dissociation smaller on one side of the jogs than on the other side, as is clearly seen in the vicinity of the extended jog.

We now consider the dynamics of the dislocations, which are set into motion by application of a shear stress σ_{xz} to the simulation cell.

2. Dislocation dynamics

We discuss first the case of the jog-free dislocation and consider its dynamics at a temperature of 100 K. This temperature is imposed to a relaxed configuration, which is equilibrated during 2 ps before application of a constant shear stress σ_{xz}. The dislocation gradually accelerates to reach a steady velocity, which depends on the applied stress as shown in Fig. 3.

The time to reach a steady velocity depends on the applied stress and varies from almost 100 ps at low stresses to about 20 ps at high stresses. Simulations in the small and large cells showed, as can be seen in Fig. 3, that the dynamics of the dislocation is independent of the cell dimensions in the X and Y directions.

The dynamics of the free dislocation is divided into two regimes, in agreement with dislocation theory[35] and previous MD simulations.[27,28] At low stresses ($\sigma<30$ Mpa), the free dislocation velocity is proportional to the applied stress. The dispersion in the phonon velocity opposes the displacement of the dislocation deformation field. A viscous friction on the dislocation results and limits the dislocation velocity. The friction coefficient per unit length, calculated from the initial slope of the free velocity at 100 K is $\nu_0=\sigma b/v = 5\times10^{-6}$ Pa s, which is a lower limit for experimental friction coefficient[35] but is of the order of the friction coefficient found by MD simulations in Ref. 28 (which is close to 3×10^{-6} Pa s).

At higher stresses, the velocity saturates close to 2.1 nm ps^{-1}, i.e., 72% of the transverse sound wave velocity (2.9 nm ps^{-1}), independently of the temperature in the range 10–100 K, and of the cell dimensions. On the other hand, this maximum velocity depends strongly on the boundary conditions applied to the $(1\bar{1}1)$ surfaces. If, for example, free-surface boundary conditions are employed, as done in Ref. 27, instead of the 2D dynamics used in the present study, the maximum velocity drops down to 1.7 nm ps^{-1}. This sensitivity shows that the maximum free dislocation velocity is controlled by processes occurring inside the $(1\bar{1}\bar{1})$ surfaces. In particular, as discussed in Ref. 36, it may be limited by the speed of the Rayleigh waves traveling along the surfaces, which certainly depends on the boundary conditions.

The dynamics of the jogged dislocation at 100 K is shown in Fig. 3. It is similar to that of the perfect dislocation, the main difference being that the jogged dislocation remains immobile for stresses up to 30 Mpa. Above this threshold, the velocity is first proportional to the applied stress, with a friction coefficient of 1.5×10^{-5} Pa s, then saturates close to the maximum free dislocation velocity. The steady structure of the gliding dislocation is similar to that shown in Fig. 9(c). The extended jog is not affected by the motion of the dislocation, while the constricted jog is strongly deformed and remains at the back of the dislocation, indicating that it is certainly a source of friction for the dislocation.

B. The interstitial clusters

1. ⟨001⟩ versus ⟨110⟩ interstitial clusters

In fcc crystals, isolated interstitials have the structure of ⟨001⟩ dumbbells. MD simulations have shown that when they cluster during displacement cascades, they adopt the ⟨110⟩ dumbbell configuration. In terms of dislocations, these clusters are small perfect dislocation loops with a Burgers vector $a/2\langle110\rangle$ aligned in the direction of the dumbbells.

We have considered clusters of various sizes, containing from 4 up to 37 interstitials, and of various shapes. We have studied their static equilibrium configuration and have computed their formation energy. These energies are compared to the formation energy of the clusters in a competing configuration, where the interstitials are grouped as dumbbells aligned in a ⟨001⟩ direction. In this case, the clusters form faulted Frank loops with a $a/3\langle111\rangle$ Burgers vector.

The interstitials are introduced in a perfect fcc lattice by placing at atomic sites in a given (111) plane (as shown in Fig. 4) an extra atom either along the ⟨110⟩ **DB** direction, or along the ⟨001⟩ **ab** direction. In the first case, the initial and the extra atoms form a pair centered around the atomic site and constitute a **DB** perfect loop. In the second case, the extra atom must be placed at mid distance between atomic sites in order to obtain a β**B** Frank loop after relaxation. The static equilibrium configuration of the clusters is obtained after a CG energy minimization, using periodic boundary conditions in all three directions of a cell of dimensions $5.2\times5\times8.5$ nm.

We have mainly considered three clusters: a 4- and a 16-interstitial diamond-shaped cluster (with edges parallel to di-

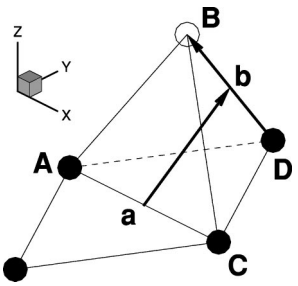

FIG. 4. Geometry of a four-interstitial cluster. The dumbbells are placed around the atomic sites which appear in black and are oriented either in direction **DB** or **ab**.

rections **DA** and **CD** of Fig. 4) and a 37-interstitial hexagonal cluster (with edges parallel to directions **DA**, **CD**, and **AC**). Their formation energies are given in Table I for both potentials, along with the formation energy of two other clusters (a 19-hexagonal and a 25-diamond shaped cluster).

The relative stability between the perfect and the Frank configuration is independent of the potential used, as found in Ref. 20, but depends strongly on the shape of the clusters. Diamond-shaped clusters of all sizes are more stable in the perfect configuration, whereas hexagonal clusters are more stable in the Frank configuration.

This point is explained by the different nature of the dislocations that form the edges of the clusters. In the case of the diamond-shaped clusters, all edges are made of glissile segments, i.e., their glide planes (which contain both their **DB** Burgers vector and their line, parallel either to the **DA** or the **CD** directions of Fig. 4) are {111} planes and form a prism along which the loop may dissociate. Dissociation is confirmed in the atomic configurations, where the hcp structure, characteristic of stacking faults, is visible across the glide planes of the segments. Dissociation is not possible in the hexagonal loops, where edges parallel to the **AC** direction are not glissile segments, but rather Lomer segments (their glide plane, which contains their **AC** line and their **DB** Burgers vector is a {001} plane) which remain constricted.

Dissociation has three consequences: (1) the energy of the perfect configuration is lowered with respect to the Frank configuration; (2) the initial dumbbells adopt a crowdionlike extended configuration and the deformation induced by the loops extends largely in the **DB** direction; (3) the plane of the loops rotates from the initial (111) plane to the (110) plane perpendicular to their Burgers vector (which minimizes the length of the loop). No such rotation is observed with the other perfect loops, in which cases, the dumbbells, keeping a compact configuration, remain centered at their initial position.

Clusters which are more stable in the perfect configuration appear as special cases, since all their edges have to be glissile segments. The clusters that form in displacements cascades have complicated shapes which do not allow any dissociation. The formation mechanism therefore favors the perfect configuration, which is locally stable at 0 K, but also at finite temperature, as will be seen in the next section. For this reason, we have included in our study clusters of different shapes, independently of their static minimum energy configuration.

We finally point out that the Burgers vector of a perfect loop may easily be determined in the atomic configurations by finding the ⟨110⟩ direction which makes the cluster invisible. We have used this method to follow the successive Burgers vector flips undergone by the loops during their interactions with the edge dislocation.

2. Dynamics of the clusters

The dynamics of ⟨110⟩ interstitial clusters will be detailed elsewhere. We only point out that they have two main characteristics. First, the clusters are highly mobile along their glide cylinder, along which they glide erratically. Their mobility decreases with their size, but remains high, even in the case of the large 37-interstitial cluster. We also note that this latter cluster is stable, at least at 100 K, with a lifetime exceeding the duration of the longest simulations, which was set to 1000 ps, even though it is not in its stable configuration.

The second characteristic of the clusters dynamics is that their Burgers vector may undergo thermally activated flips from one $a/2\langle 110\rangle$ direction to another one. The energy barrier to Burgers vector flip was estimated in the case of the four-interstitial cluster, using a reaction coordinate algorithm, and a value of 0.45 eV was found, in agreement with previous estimates.[12]

IV. CLUSTERS INITIALLY BELOW THE DISLOCATION

We now examine the behavior of the interstitial clusters in the presence of an edge dislocation. We consider first the case of the jog-free dislocation and focus on clusters having a **DB** Burgers vector, perpendicular to the dislocation Burgers vector. Results concerning clusters with a **DA** Burgers

TABLE I. Formation energy of the clusters in the perfect and Frank configurations, using the potentials developed by Angelo *et al.* (Ni1) and Mishin *et al.* (Ni2). Are also given in the table: the approximate radius of the cluster and their shape (D for diamond-shaped and H for hexagonal).

SIA	Radius (nm)	Shape	Formation Energy (eV)			
			Ni1		Ni2	
			Perfect	Frank	Perfect	Frank
4	0.2	D	11.6	12.0	14.8	15.6
16	0.5	D	28.9	31.8	34.8	37.2
19	0.5	H	35.3	34.1	43.2	39.1
25	0.7	D	39.2	42.7	45.6	48.9
37	0.8	H	54.3	52.6	64.5	58.4

TABLE II. Dislocation capture distance at 0 K and binding energy of the clusters to the dislocation in different configurations, obtained with Angelo's potential.

SIA	Capture distance (nm)	Binding energy (eV) as **DA** loops	as superjogs
4	1.8	6.0	
16	2.8	15.4	16.9
19		18.1	19.1
25		21.6	
37	3.2	27.6	34.8

vector, parallel to the dislocation glide plane, were presented elsewhere.[23] We consider a configuration where a cluster is initially placed below the stacking fault ribbon of the dislocation.

A. Initial absorption reaction

The simulation cell used is that of Fig. 1. We have considered the different clusters described in the previous section. For each simulation, a cluster is introduced in the cell containing the relaxed dislocation in the same way as before: pairs of atoms pointing in the **DB** direction are introduced around atomic sites lying in a given (111) plane, below the stacking fault ribbon of the dislocation. An initial CG energy minimization leads to the relaxed structure of the cluster.

In summary, the simulations show (1) that there exists a critical distance from the dislocation glide plane below which the loop is spontaneously attracted to the dislocation, (2) that when the loop is attracted, it is absorbed in one of the Shockley partials of the dislocation, the absorption being assisted by a flip of the loop Burgers vector, and (3) that once the cluster is absorbed, it forms locally an energetically favorable junction with the dislocation. We discuss successively these three points in the remainder of this section.

If the interstitials are placed further than a critical distance from the dislocation glide plane, called the *capture distance of the dislocation*, they relax during the initial energy minimization to form the loops expected in absence of the dislocation. On the other hand, if the initial distance is less than the capture distance, the cluster is unstable during the relaxation and spontaneously glides in the direction of the dislocation. The capture distance of the dislocation at 0 K, evaluated from the simulations when the clusters are close to the central (YZ) plane, increases with the size of the clusters and is given in Table II for the three main clusters.

The capture distance also increases with the temperature. There exists at 100 K a distance below which the clusters spontaneously glide in the direction of the dislocation as soon as the dynamics are imposed, and above which they are not attracted to the dislocation, at least during the duration of the simulations. The 100 K capture distance was evaluated precisely in the case of the four-interstitial cluster and is equal to 3.5 nm, therefore greater than at 0 K.

When the cluster is attracted to the dislocation at 100 K, it glides until it reaches the dislocation glide plane and stops at that position. The Burgers vector of the cluster then flips within 1 ps from the **DB** vector to either the **DA** or the **CD** vector. This flip is due, at the atomic-level, to a rotation of the dumbbells of the clusters from the initial ⟨110⟩ direction to a new ⟨110⟩ direction. The flip direction depends on the position of the clusters with respect to the partials: the Burgers vector flips towards **DA** (respectively **CD**) when the cluster is closer to the **A**β (respectively β**C**) partial.

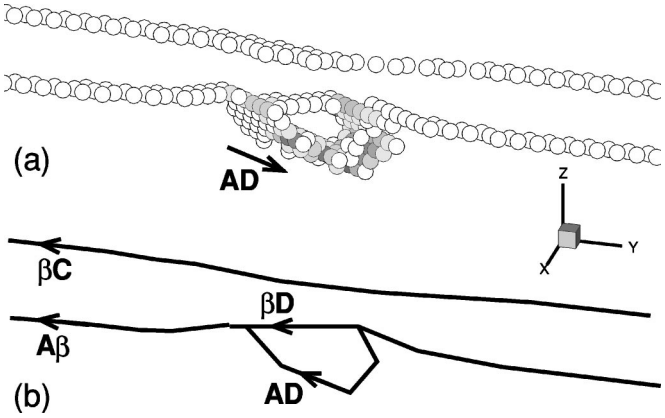

FIG. 5. Dislocation structure after absorption of a 37-interstitial cluster (a), and corresponding Burgers vector geometry (b). The color of the atoms in (a) scales with their energy: darker atoms have a higher energy.

After the Burgers vector flip, part of the cluster is in the dislocation glide plane. It glides along its new Burgers vector towards the closest partial and stops only when it is in contact with the latter. The relaxed structure in the case of the 37-interstitial cluster is shown in Fig. 5, where the partials and the defect cluster are clearly visible. Figure 6 is a projection of the dislocation perpendicularly to the **DA** direction, aligned with the cluster Burgers vector. We note that the cluster being a perfect dislocation loop, its central region is only elastically deformed and the atoms in this region, having a low energy, do not appear in the figure.

This atomic-level structure may be interpreted in terms of dislocation lines with Burgers vectors as shown in Fig. 5(b). The loop forms a junction with the partial dislocation, according to the reaction: **DA**+**A**β=**D**β. If its Burgers vector were **CD**, it would form a junction with the β**C** partial according to the reaction: **CD**+β**C**=β**D**. These junctions are energetically favorable according to Frank's rule,[37] which explains why the loops are attracted to the corresponding partial rather than the other one.

It can be seen in Fig. 6 that the shape of the loop, which was initially hexagonal, has changed during the interaction. Such a change of shape will be discussed in detail in a later section, when the loop is absorbed on the dislocation in the form of a double superjog.

The binding energy of the cluster to the dislocation is defined as the balance between, on the one hand, the sum of

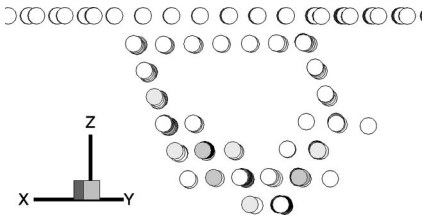

FIG. 6. Projection of the dislocation perpendicularly to the cluster Burgers vector. The color of the atoms scales with their energy.

the energies of the present configuration plus that of the defect free cell, and, on the other hand, the sum of the energies of the cell with the dislocation alone plus that with the cluster alone placed at a reference position. It is independent of the cell dimensions and of the reference position of the cluster as long as the latter is not too close to the (111) surfaces. Because of the symmetry between the two possible final configurations, the binding energy found in both cases is the same and is given in Table II for the different clusters considered. The magnitude of these energies implies that the clusters cannot escape as a whole by thermal activation.

In order to check the sensitivity of the results to the interatomic potential, the same calculations were performed with the EAM potential developed by Mishin *et al.*[26] with the result that the same reactions were observed. The possibility of Burgers vector flip in the vicinity of the dislocation stacking fault ribbon therefore does not depend on the potential used and is possible even for loops of radius as large as about 1 nm.

B. Influence of the clusters on the dislocation dynamics

We now consider the response of the dislocation containing a cluster to an applied shear stress and consider first the case of the four-interstitial cluster with a **DA** Burgers vector. We examine the case of the large simulation cell, keeping in mind that the same behavior was observed in the small cell as well.

The initial configuration is the static configuration considered above, equilibrated at 100 K before application of a shear stress. If a stress below 120 Mpa is applied, the dislocation gradually accelerates to reach a steady velocity, dragging along the loop in much the same way as a classical jog. The loop glides in the direction of its own **DA** Burgers vector, at 60° from the glide direction of the dislocation. It therefore *travels along* the dislocation line. The partial containing the loop bows out between the defect and its periodic images, with a steady curvature which increases with the applied stress. Correspondingly, the steady distance between the loop and the back partial decreases until, at 120 Mpa, a constriction occurs between the partials.

Figure 7 shows the configuration of the dislocation before, during, and after the constriction. During the initial acceleration phase [Fig. 7(a)], the loop is dragged in the **AD** direction and the distance between the loop and the back partial gradually decreases, until this dislocation is in contact with the defect cluster, resulting in a constriction of the dislocation [Fig. 7(b)]. This configuration is unstable and the front partial breaks away, leaving the loop inside the core of the back partial. The loop remains attached to the back partial and adopts a new Burgers vector, the **AC** vector parallel to the glide direction [Fig. 7(c)]. It is then dragged in this direction by the dislocation, which reaches a steady velocity. The binding energy is 5.3 eV for this latter configuration, i.e., lower than before the change of Burgers vector. At still higher forces (300 Mpa), unpinning is observed: the loop is left behind the dislocation and keeps its **AC** Burgers vector.

We now turn to the evolution of the dislocation terminal velocity as a function of the applied stress and applied force, as shown in Fig. 8. This force is the total force applied to the dislocation between a loop and its periodic images and is

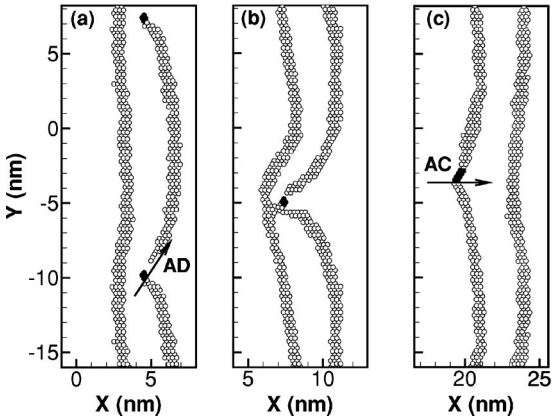

FIG. 7. Snapshots of the dislocation at 150 Mpa, 100 K after, respectively, 3 ps (a), 9 ps (b), and 15 ps (c). The dumbbells appear in black. The vectors indicate the Burgers vector of the loop. The figure includes part of the periodic image of the dislocation.

therefore equal to the product σbl, where l is the distance between loops ($l=L_y$ in the present case).

The dislocation is never locked by the clusters which, nevertheless, are sources of extra friction for the dislocation. The initial friction on the dislocation depends on the density of clusters along its line (b/l) and is well approximated by the law: $\nu_{eff}=\nu+b/l\ \nu_b$, where ν is the friction coefficient of the dislocation in absence of the loops (calculated before) and $\nu_b=17.3\times10^{-5}$ Pa s. The effective friction on the dislocation in presence of the clusters therefore increases linearly with the clusters density.

The jump in the dislocation velocity, visible in Figs. 8(a) and 8(b), corresponds to the rearrangement of the loop inside the dislocation core described above. As seen in Fig. 8(b), it occurs at a constant applied force σbl (equal to 3 eV nm^{-1} in the case of the four-interstitial cluster). Below this threshold force, the steady velocity saturates at 0.9 nm ps^{-1}. Since the loop has a Burgers vector at 60° from that of the dislocation, it travels twice as fast as the dislocation. Its velocity reaches 1.8 nm ps^{-1} which is the highest velocity reached by a loop in all our simulations, and is close to the maximum free velocity. The plateau may therefore be explained by a relativistic saturation of the loop velocity, as considered in

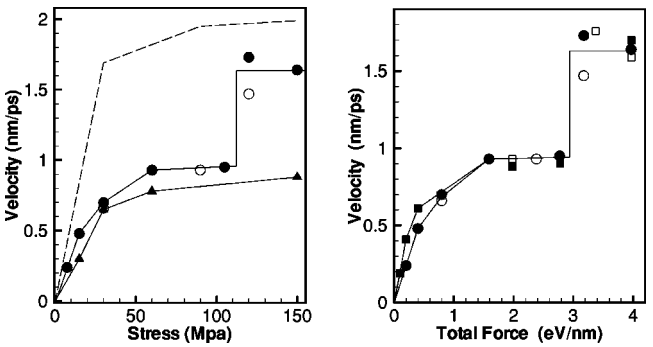

FIG. 8. Dislocation velocity as a function of applied stress (a) and applied force (b). The dashed curve corresponds to the free dislocation. Squares and circles correspond to the four-interstitial cluster in the small and large cells, and triangles, to the 16-interstitial cluster in the large cell. Empty symbols were obtained at 10 K; full symbols, at 100 K.

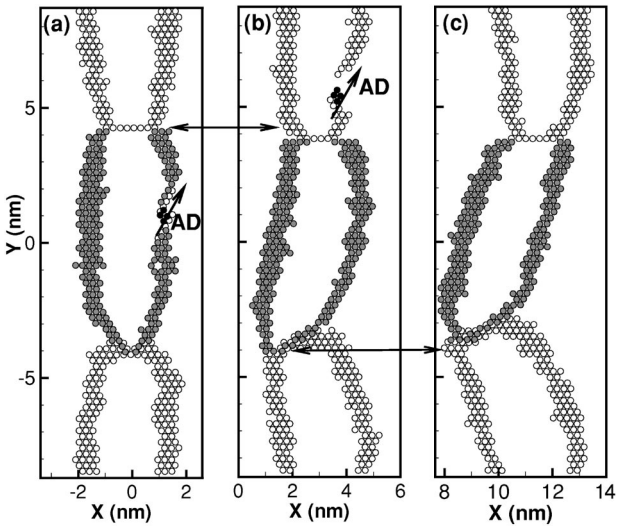

FIG. 9. Snapshots of the jogged dislocation at 90 Mpa and 100 K, after, respectively, 0 ps (a), 7 ps (b), and 19 ps (c). The dumbbells appear in black, while core atoms in the upper and lower glide planes appear, respectively, in gray and white. The vectors indicate the Burgers vector of the cluster.

the case of jog drag:[38] the defect cluster has reached its maximum velocity and limits the velocity of the dislocation. Beyond the threshold force, the loop rearranges as described above and glides in the same direction as the dislocation and therefore at the same velocity. The dislocation velocity is no longer limited to 0.9 nm ps^{-1}, and, as seen in Fig. 8, jumps up to 1.6 nm ps^{-1}. This velocity is lower than the free velocity which implies that the **AC** loop is also a source of additional friction for the dislocation glide.

The 16- and 37-interstitial clusters are also dragged by the dislocation along their Burgers vector and have a similar influence on the dislocation dynamics as the four-interstitial cluster. The velocity of the dislocation containing a 16-interstitial cluster is shown in Fig. 8(a). The initial friction coefficient is 1.25×10^{-5} Pa s, higher than in previous case. On the other hand, the saturation velocity is unchanged and a dynamical constriction is also observed but for stresses above 150 Mpa. No Burgers vector flip then occurs; the cluster rather unpins from the dislocation and is left behind, keeping its initial **DA** Burgers vector.

C. Case of the jogged dislocation

We now discuss the interactions between the double jogged dislocation described above and the four-interstitial cluster. Initial absorption of the cluster is not influenced by the presence of the jogs. The configuration after absorption is shown in Fig. 9(a), which was obtained by applying the dynamical visualization method to both the upper and lower glide planes. This configuration is similar to the one obtained with the jog-free dislocation:[23] two of the four dumbbells lie in the upper glide plane, while the two others are in the plane just below.

Starting form this configuration, a stress $\sigma=90$ Mpa is applied which accelerates the dislocation. As in previous cases, the cluster is dragged along its **DA** Burgers vector, travels along the dislocation, and approaches the extended jog. When the cluster reaches this jog, the two interstitials lying in the upper glide plane are absorbed by the jog within 1 ps. During the absorption, the jog is much disturbed and tends to constrict in order to absorb the interstitials. As expected from dislocation theory, absorption of two interstitials causes the jog to advance by two [110] atomic rows, as indicated by the arrows between Figs. 9(a) and 9(b). The two remaining dumbbells can be seen in the lower glide plane beyond the extended jog in Fig. 9(b). They have kept their initial **DA** direction.

The dislocation continues to glide, dragging along the remaining interstitials, which soon reach the constricted jog and are absorbed. As before, the jog advances by two atomic [110] rows, as shown in Fig. 9(c). The dislocation then reaches a steady velocity of 1 nm ps^{-1}, exactly equal to its velocity in absence of the cluster (see Fig. 3).

The reactions observed here were expected from dislocation theory. With respect to irradiation hardening, they point to a *dynamical recovery mechanism* for the dislocation, whereby the irradiation defects absorbed by the dislocation are eliminated while the latter is gliding.

V. CLUSTERS INITIALLY AHEAD OF THE DISLOCATION

We consider now a new configuration where the clusters interact with the edge dislocation while the latter is gliding. In this case, the **DB** cluster is placed in a given $(1\bar{1}1)$ plane 4 nm ahead of the dislocation, 1 nm above its glide plane. Upon initial energy minimization, the interstitials relax to form the loop expected in absence of the dislocation. A temperature of 100 K is then applied to the system, which is equilibrated before application of a low shear stress ($\sigma=15$ Mpa), which drives the dislocation in the direction of the cluster.

The simulations show that the dislocation and the cluster may interact in different ways, depending on the initial distribution of atomic velocities. Therefore the system may follow different dynamical trajectories which have similar probabilities for the given conditions of temperature and applied stress (100 K, 15 Mpa). In all cases, the loop stabilizes just above the glide plane as the dislocation arrives. It then passes below the glide plane and, depending on the simulation, may or may not interact with the dislocation. When dislocation and loop do not interact, the loop simply remains below the glide plane while the dislocation passes by. When they interact, the Burgers vector of the loop systematically flips to one of the three $a/2\langle110\rangle$ vectors parallel to the dislocation glide plane. The loop may therefore react with the front $\mathbf{A}\beta$ partial and become a **DA** loop. It may also not interact with the front partial, but react with the back partial and become a **CD** loop. In these first two cases, the final configurations are similar to those described in the previous section: the loop is attached to the partial dislocation by means of a junction. A third interaction mechanism is possible: the loop interacts with the $\mathbf{A}\beta$ partial and its Burgers vector flips to **AC**, leading to the absorption of the loop on the dislocation in the form of a *double superjog*.

The three different structures have been obtained with the 16- and 37-interstitial clusters, but also with intermediate 18-, 19-, and 23-interstitial clusters, which shows that, in the general case, all three final Burgers vector are equally likely.

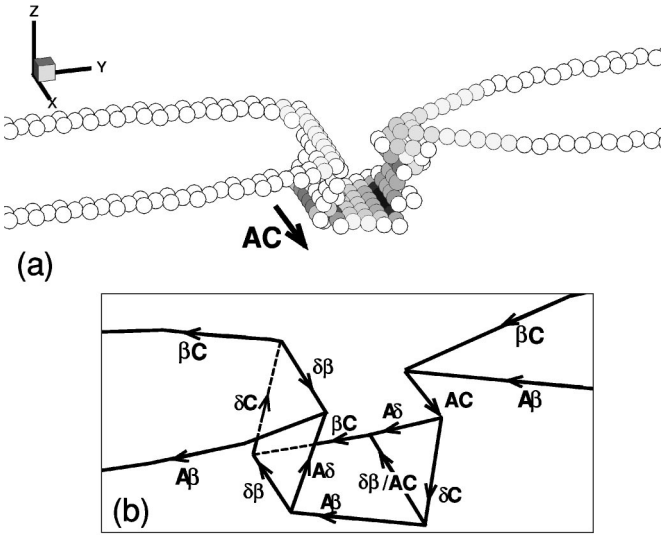

FIG. 10. Dislocation structure after formation of a double superjog (a) and corresponding Burgers vector geometry (b). The color of the atoms in (a) scales with their energy.

On the other hand, double superjogs were not obtained with the clusters containing 4 and 25 interstitials. The Burgers vector of the four-interstitial cluster may rotate to the **AC** direction, but the cluster remains attached to the front partial in a configuration symmetrical to that shown in Fig. 7(c). The disturbance induced by the loop is not sufficient to induce the constriction of the partials necessary to the formation of the superjogs. The Burgers vector of the 25-interstitial cluster has not been observed to flip towards the **AC** direction. Therefore in the special case of this cluster and for a reason which remains unclear, the probability of rotation towards **AC** is much lower than towards the other directions.

The first two interaction mechanisms were described in the previous section. We describe here the third mechanism and focus on the case of the 37-interstitial cluster, keeping in mind that similar reactions occur with the other clusters. The effect of the superjogs on the dislocation dynamics is considered later on.

A. Formation of a double superjog

The interaction process lasts 2 ps and is rather complicated at the atomic level. Given some simplifications, it can be interpreted in terms of continuous dislocations in the following way. When the loop comes into contact with the front partial, the dumbbells rotate towards the **AB** direction (see Fig. 1). Loop and dislocation therefore form a $\mathbf{A}\beta+\mathbf{BA}=\mathbf{B}\beta$ junction. The plane of the loop rotates from ACD to BCD. A constriction then occurs at the level of the junction, forming a $\beta\mathbf{C}+\mathbf{B}\beta=\mathbf{BC}$ segment, which sweeps out the **AB** loop and transforms the latter into an **AC** loop. The net result is therefore the rotation of the Burgers vector of the loop from **DB** to **AC** and the absorption of the latter as an *indentation* on the dislocation. The relaxed configuration obtained in the case of the 37-interstitial loop is shown in Fig. 10. This structure is the equivalent for an edge dislocation of the helicoidal turns that form on screw dislocations.[10] Figure 11(a) is a projection of the structure perpendicularly to the **AC** direction, parallel to the dislocation Burgers vector.

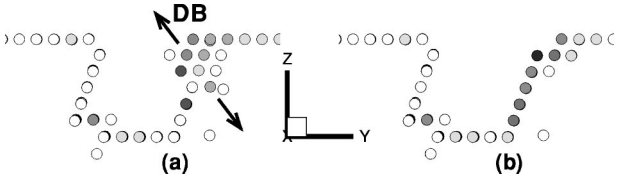

FIG. 11. Projection of the double superjog perpendicularly to the X direction before unpinning of the dislocation (a), and after (b). The color of the atoms scales with their energy.

The shape of the cluster has changed during the interaction, so that the cluster has been transformed into a *double superjog* on the dislocation. Figure 10(a) shows that one superjog is extended, while the other is constricted, as was observed in Sec. III, in the case of unit jogs. The segment between the superjogs has climbed down six $(1\bar{1}1)$ planes and contains itself a unit jog on the left-hand side, as seen in Fig. 11(a). It is extended in its new ACD glide plane.

The structure, interpreted in terms of dislocation lines, is shown in Fig. 10(b). As said previously, dissociation of the extended superjog in its ABC plane produces two $\delta\beta$ Lomer-Cottrell stair-rod dislocations, visible on the left-hand side of Fig. 10(b). The structure of the other superjog is more complicated. The superjog is dissociated in its lower part, with the formation of a $\delta\beta/\mathbf{AC}$ stair-rod segment. The rest of the superjog is constricted. Careful analysis of the atomic configuration reveals that it is made of a Lomer segment, which characteristic fivefold symmetrical core, aligned in the $[1\bar{1}0]$ **DB** direction, can be followed over three $(1\bar{1}1)$ planes, as noted in Fig. 11(a).

Similar double superjogs have been obtained with other clusters. Their formation energies are given in Table II. They are systematically energetically more favorable than the corresponding structure with a final **DA** or **CD** Burgers vector. We also note that Lomer segments have been observed in all cases and play a crucial role in the dislocation dynamics, as shown in the following section.

B. Pinning and unpinning mechanisms

Unlike the cases where the final Burgers vector of the loops is in the **DA** or **CD** direction, the double superjogs lock the dislocation: there exists a critical stress below which the dislocation is pinned. This stress is well defined at 0 K and was estimated by static simulations to be 180 Mpa, in the case of the 37-interstitial loop in the large simulation cell. At finite temperature, unpinning becomes stochastic, and depends on the initial distribution of atomic velocities. We discuss this point in the next section and focus for the time being on the dislocation pinning and unpinning mechanisms at the atomic level.

Figure 12(a) shows the dislocation 7 ps after the beginning of a simulation, made at 100 K with an applied stress of 150 Mpa. The figure presents the part of the dislocation lying in its initial glide plane. The segment which has climbed is behind the plane of the figure and leaves inside this plane a region of perfect crystal. The dissociated superjog, which was initially centered around $x=3.5$ nm, has glided forward, while the constricted superjog remained immobile. The dis-

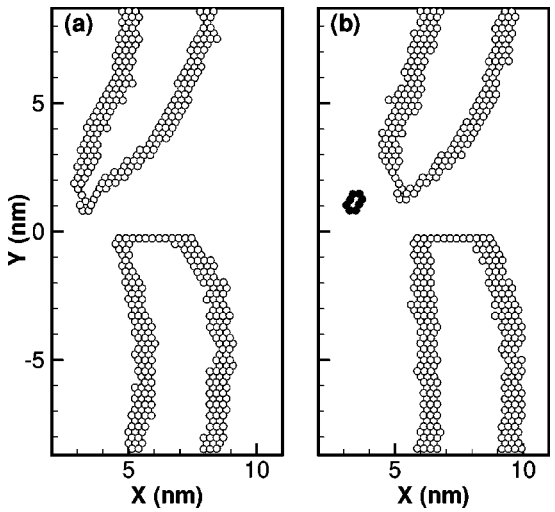

FIG. 12. Dislocation at 150 Mpa and 100 K after, respectively, 7 ps (a) and 10 ps (b). Two vacancies, left after unpinning of the dislocation, are seen in (b), surrounded by black atoms.

location is pinned at the level of this superjog. The pinning is due to the presence of the Lomer segment: this segment is known to have a low mobility because the Peierls stress in its {001} glide plane is high. The force applied by the dislocation on the segment is not sufficient to overcome the Peierls stress and set the segment into motion.

Figure 12(b) shows the dislocation, 3 ps later. It has unpinned and the unpinning mechanism involved the destruction of the Lomer segment. This mechanism also occurs in static simulations. The Lomer segment is destroyed by incorporation of three interstitials in the constricted superjog. When the dislocation unpins, three vacancies are left at the position of the initial Lomer segment. Two of them, lying in the dislocation glide plane, are visible in Fig. 12(b). The three interstitials corresponding to the three vacancies are absorbed by the dislocation and serve to transform the Lomer segment into a glissile segment. Figure 11(b) shows the relaxed structure of the double jog after unpinning. It is unchanged except in the region of the Lomer segment, where it can be seen that the glissile $\mathbf{A}\delta + \delta\mathbf{C}$ segment now extends up to the main glide plane. The motion of the dislocation after unpinning is fast and continuous: the dislocation reaches a velocity of 0.55 mn ps^{-1} for an applied stress of 150 Mpa. The mobility of the dislocation in this new configuration was checked by relaxing the present configuration with no applied stress before applying back a stress of 150 Mpa. The dislocation starts to glide as soon as the dynamics are applied, which confirms that the dislocation was pinned by the Lomer segment.

We have observed a second unpinning mechanism, which is simply the glide of the Lomer segment inside its own glide plane. This means that the force applied by the dislocation on the Lomer segment, helped by thermal activation, reaches the Peierls stress. This glide motion is slow and discontinuous: the segment advances by one Peierls valley every approximately 5 ps which corresponds to 0.05 nm ps^{-1}.

C. Thermal activation of the dislocation unpinning

We have started to study the influence of the temperature on the unpinning stress and mechanism. Our first simulations show that the dislocation unpins at finite temperature, at applied stresses lower than the static unpinning stress: at 600 K, unpinning is observed at applied stresses down to 120 Mpa. However, for given conditions of stress and temperature, both the occurrence of unpinning, and the unpinning mechanism depend on the initial atomic velocities. Thus, depending on these velocities, the dislocation may or may not unpin within the duration of the simulations (which was set to 15 ps), and if it unpins, it may start gliding by glide or destruction of the Lomer segment. Moreover, large scatters are observed in the time intervals before unpinning. More simulations are needed in order to characterize the role played by temperature in the unpinning process of the dislocation.

VI. DISCUSSION

In this section, the results of the simulations are summarized and discussed with respect to their interest for the atomic-scale study of plasticity in irradiated fcc crystals.

A. Structure and glide of the edge dislocation

The present work leads to a detailed analysis of the atomic-scale structure of an edge dislocation in different configurations involving unit jogs, superjogs, and small junctions, both in static and dynamic situations. These structures can be compared to TEM observations. Along with previous MD simulations of dislocation dynamics,[28,39,40] they point out the realism of the simulation of dislocations from the atomic scale, although only semiempirical EAM potentials are used.

We have seen that the main characteristics of the dislocation structures can be explained by considering the latter as made of dislocation line segments and using simple elastic arguments, based on the line tension of the segments. However, we have also seen that atomic resolution is needed to determine the structures in details. In particular, the presence of a sessile Lomer segment along the constricted superjogs, which is of importance for the mobility of the dislocation, as described in the above section, could not be predicted in absence of atomistic simulations.

MD simulations also allow to study the dynamics of the dislocation. We have seen that jogs (particularly, constricted jogs) can lock the dislocation and are sources of viscous friction on the dislocation, with friction coefficients of the order of those found experimentally. We have also seen that the dislocation reaches the relativistic regime for applied stresses relatively low, of the order of 100 Mpa. As a consequence, dislocations in real specimens, gliding freely between obstacles, are expected to reach velocities close to the sound velocity, which points out the interest of studying dislocations in the relativistic regime.

B. Contact interactions between the edge dislocation and interstitial clusters

The main objective of the present work was to study the behavior of interstitial clusters in the presence of an edge dislocation. We have considered various clusters and have shown that their static equilibrium configuration (either Frank or perfect loop configuration) depends strongly on

their shape and size. On the other hand, simulations at finite temperature show that perfect loops of all shapes and sizes are locally stable at 100 K, even if they are not in their static minimum energy configuration. Their mobility decreases when their size increases but remains high, even in the case of the 37-interstitial cluster. We have also noted that their Burgers vector is not well defined, since it may undergo thermally activated flips from one perfect orientation to another one.

The interaction mechanisms between the dislocation and the clusters, and the resulting structures, are independent of the size and shape of the loops, except in some special cases. This is partly due to the fact that the shape of the loops strongly changes during the interactions, such that two clusters, initially different, may lead to very similar structures.

A key result of the simulations is to show that the loop Burgers vector becomes unstable when the loop comes into contact with the dislocation and flips systematically towards one of the three $a/2\langle 110\rangle$ Burgers vector parallel to the dislocation glide plane (**DA**, **CD**, or **AC**). On the other hand, when the loops are initially placed ahead of the dislocation, the precise direction of flip among these three directions is not well defined and depends on the dynamical trajectory of the system. The resulting structure may therefore not be the static equilibrium structure of the system. When the final Burgers vector is either **DA** or **CD**, the cluster is attached to one of the Shockley partials of the dislocation by means of a junction. In the third case, the cluster is absorbed in the form of a double superjog.

It is therefore excepted that an edge dislocation, gliding across a population of interstitial clusters, will *polarize* the cluster Burgers vectors in a direction parallel to its glide plane, i.e., all loops lying within the capture distance of the dislocation will adopt a Burgers vector parallel to its glide plane. We have seen such a process in the case of **DB** loops. Although the simulations have not been performed directly, **AB** and **CB** loops are expected to undergo similar flips; notice that the other possible Burgers vectors are already parallel to the dislocation glide plane.

C. Glide of the edge dislocation containing interstitial clusters

The simulations show that only double superjogs lock the dislocation, the locking effect being due to the presence of a Lomer segment in the constricted superjog. Hirsch[7] showed that Lomer segments may form when loops of particular shapes are absorbed on screw dislocations as helicoidal turns. In the present simulations, Lomer segments form independently of the initial cluster shape, since the latter changes strongly during the interaction. Hirsch considered the pinning effect due to these segments and suggested that the dislocation may unpin by an Orowan looping process or by the thermally activated glide of the Lomer segment. We have not seen the first mechanism, but have observed another mechanism, which involves the destruction of the Lomer segment by absorption of interstitials. We note again that this type of information can only be obtained by atomic methods, since it depends on atomic-level reactions. Once the dislocation glides, the loops, independently of their configuration, are sources of viscous friction on the dislocation.

In all cases, the final Burgers vector of the loops being parallel to the dislocation glide plane, the loops follow the dislocation in its motion and are removed from their initial position. We also note that loops away from the dislocation glide plane, with a Burgers vector parallel to the latter, are also dragged by the dislocation, as was shown previously,[23] in agreement with elastic calculations.[6] This *sweeping mechanism* certainly contributes to the formation of the *clear bands* observed experimentally in deformed irradiated materials: the shear bands, along which the deformation is localized, are nearly clear of any irradiation defect after deformation, showing that the defects are swept out by the gliding dislocations.

The loops attached to the dislocation are therefore removed from their initial position. They may then be eliminated from the dislocation line. Loops with a final Burgers vector different from that of the dislocation (either **CD** or **DA**) *travel along* the dislocation while the latter glides, and may reach other defects located along the dislocation line. These defects may be other absorbed loops, leading to coalescence between these loops and the moving clusters. They may also be unit or superjogs. In this case, the loops are eliminated from the dislocation line by absorption at the jogs, as seen in the case of the four-interstitial loop attached to the double-jogged dislocation. The motion of the clusters along the dislocation line therefore leads to a *dynamical recovery* of the dislocation. This conclusion agrees with TEM observations made by Sharp[13] in a study of the clear bands in nickel crystals. This author noted that the irradiation defects removed from the clear bands are not pushed towards the edges of the bands but are eliminated from the material, as is seen in the simulations. Moreover, the author noted that mobile dislocations have less jogs along their lines than immobile ones. This is consistent with the fact that when jogs or superjogs absorb interstitial clusters, they also move along the dislocation line and may coalesce.

The formation of the superjogs on the edge dislocation is relevant with respect to a third observation made by Sharp. This author observed that a clear band forms by nucleation of an initial slip plane, which then broadens by double cross slip. The present simulations point to another possible broadening mechanism, which involves the superjogs. The formation of a double superjog on an edge dislocation plays in fact a role similar to the double cross slip of a screw dislocation: the part of the dislocation which climbs between the superjogs lies in a new slip plane parallel to the initial one, where it can act as a new dislocation source, thus leading to a broadening the clear band.

D. Hardening by the interstitial loops

DA and **CD** loops do not lock the dislocation. Therefore they do not participate in the increase of yield stress observed experimentally. On the other hand, since they slow down the dislocation, they play a role in irradiation hardening via the deformation rate sensitivity of the irradiated material. Double superjogs lock the dislocation, but the hardening effect is small, since the yield stress at 0 K increases up to only 180 Mpa, whereas the experimental increase is of the order of 300 Mpa for irradiation defect densities smaller than in present case.

Therefore the small dislocation loops considered in the present article represent rather weak dispersed barriers. They may still play a role in source hardening. In order to study

further this mechanism, the formation of defect structures (*clouds*) around the dislocation has to be examined, which implies to consider the behavior of multiple defects in the vicinity of the dislocation. A straightforward way would be to use MD simulations of displacement cascades. Such cascades could be performed near a dislocation and defect clustering around the dislocation could be followed during the cascade. Another possibility would be to drive a dislocation across a defect microstructure produced by a cascade, in order to examine the reorganization of the defects induced by the presence of the dislocation.

VII. CONCLUSION

The simulations presented here focus on elementary processes occurring when a small interstitial loop comes into contact with an extended edge dislocation in an EAM nickel crystal. The picture drawn from the simulations is the following. A dislocation, gliding across a field of interstitial clusters, absorbs the clusters lying within its capture distance. These clusters adopt a Burgers vector parallel to its dislocation glide plane and may therefore be dragged away. While being dragged, they travel along the dislocation line and are eliminated either by coalescence with other absorbed clusters or by absorption at unit or superjogs. The dislocation may also sweep the clusters towards vacancy clusters, leading to the recombination of the interstitials with the vacancies. The dislocation is therefore, at the same time, a center for dynamical recombination, coalescence, and elimination at jogs.

From a more fundamental point of view, the unpinning mechanism of the double superjogged dislocation appears to be a process where thermal activation can be studied in detail, by means of simple MD techniques. This study should lead to a better understanding of the role played by temperature in atomic processes, but also of the role played by the dissipation induced by the dislocation, which is included in the classical theories of thermal activation only in an approximated way.

ACKNOWLEDGMENTS

The authors thank Dr. N. V. Doan for his help in the MD simulations. They are grateful to Professor Y. Bréchet and Dr. Y. Le Bouar for many insightful discussions.

[1] A. W. McReynolds, W. Augustiniak, M. McKewon, and D. B. Rosenblatt, Phys. Rev. **98**, 418 (1955).
[2] T. H. Blewitt, R. R. Coltman, R. E. Jamison, and J. K. Redman, J. Nucl. Mater. **2**, 277 (1960).
[3] J. Diehl, in *Vacancies and Interstitials in Metals*, edited by A. Seeger (North-Holland, Amsterdam, 1969), p. 739.
[4] F. Kroupa, Philos. Mag. **7**, 783 (1962).
[5] R. L. Fleischer, Acta Metall. **10**, 835 (1962).
[6] M. J. Makin, Philos. Mag. **10**, 695 (1964).
[7] P. B. Hirsch, in *Vacancies '76*, edited by R. E. Smallman and J. E. Harris (The Metals Society, London, 1977), p. 95.
[8] G. Saada and J. Washburn, J. Phys. Soc. Jpn. **18**, Suppl. 1, 43 (1963).
[9] D. Kuhlmann-Wilsdorf, Philos. Mag. **49**, 125 (1958).
[10] J. L. Strudel and J. Washburn, Philos. Mag. **9**, 491 (1964).
[11] A. Seeger, in *Proceedings of the 2nd UN International Conference on Peaceful Uses of Atomic Energy* (United Nations, Geneva, 1958), Vol. 6, p. 250.
[12] H. Trinkaus, B. N. Singh, and A. J. E. Foreman, J. Nucl. Mater. **249**, 91 (1997).
[13] J. V. Sharp, Philos. Mag. **16**, 77 (1967).
[14] T. Diaz de la Rubia and M. W. Guinan, Phys. Rev. Lett. **66**, 2766 (1991).
[15] A. J. E. Foreman, W. J. Phythian, and C. A. English, Philos. Mag. A **66**, 671 (1992).
[16] D. J. Bacon, A. F. Calder, and F. Gao, J. Nucl. Mater. **251**, 1 (1997).
[17] N. V. Doan and R. Vascon, Nucl. Instrum. Methods Phys. Res. B **135**, 207 (1998).
[18] R. S. Averback and T. Diaz de la Rubia, Solid State Phys. **51**, 281 (1998).
[19] A. J. E. Foreman, C. A. English, and W. J. Phythian, Philos. Mag. A **66**, 655 (1992).
[20] Yu. N. Osetsky, M. Victoria, A. Serra, S. I. Golubov, and V. Priego, J. Nucl. Mater. **251**, 34 (1997).
[21] M. Kiritani, J. Nucl. Mater. **251**, 237 (1997).
[22] B. N. Singh, A. J. E. Foreman, and H. Trinkaus, J. Nucl. Mater. **249**, 103 (1997).
[23] D. Rodney and G. Martin, Phys. Rev. Lett. **82**, 3272 (1999).
[24] J. E. Angelo, N. R. Moody, and M. I. Baskes, Modell. Simul. Mater. Sci. Eng. **3**, 289 (1995).
[25] M. I. Baskes, R. G. Hoagland, and T. Tsuji, Modell. Simul. Mater. Sci. Eng. **6**, 9 (1998).
[26] Y. Mishin, D. Farkas, M. J. Mehl, and D. A. Papaconstantopoulos, Phys. Rev. B **59**, 3393 (1999).
[27] M. S. Daw, M. I. Baskes, C. L. Bisson, and W. G. Wolfer, in *Modeling Environmental Effects on Crack Growth Processes*, edited by R. H. Jones and W. W. Gerberich (The Metallurgical Society, Warrendale, PA, 1986), p. 99.
[28] M. S. Daw, S. M. Foiles, and M. I. Baskes, Mater. Sci. Rep. **9**, 251 (1993).
[29] A. Aslanides and V. Pontikis, Comput. Mater. Sci. **10**, 401 (1998).
[30] M. P. Allen and D. J. Tildesley, *Computer Simulation of Liquids* (Clarendon Press, Oxford, England, 1987), p. 228.
[31] C. B. Carter and S. M. Holmes, Philos. Mag. **35**, 1161 (1977).
[32] P. M. Hazzledine, H. P. Karnthaler, and E. Wintner, Philos. Mag. **32**, 81 (1975).
[33] P. B. Hirsch, Philos. Mag. **7**, 67 (1962).
[34] T. Rasmussen, K. W. Jacobosen, T. Leffers, and O. B. Pedersen, Phys. Rev. B **56**, 2977 (1997).
[35] V. I. Alshits and V. L. Indenbom, in *Dislocations in Solids*, edited by F. R. N. Nabarro (North-Holland, Amsterdam, 1986), Vol. 7, p. 43.
[36] J. P. Hirth and J. Lothe, *Theory of Dislocations*, 2nd ed. (Krieger, Malabar, 1992), p. 192.
[37] F. C. Frank, Physica (Utrecht) **15**, 131 (1949).
[38] J. Friedel, *Dislocations* (Pergamon Press, Oxford, 1964), p. 119.
[39] V. Bulatov, F. Abraham, L. Kubin, B. Devincre, and S. Yip, Nature (London) **391**, 669 (1998).
[40] S. J. Zhou, D. L. Preston, P. S. Lomdahl, and D. M. Beazley, Science **279**, 1525 (1998).